Variable density and viscosity, miscible displacements in horizontal Hele-Shaw cells. Part 2. Nonlinear simulations

M. O. John[1,2], R. M. Oliveira[2], F. H. C. Heussler[2,3] and E. Meiburg[2],†

[1]ETH, Institute of Fluid Dynamics, CH-8092 Zurich, Switzerland

[2]Department of Mechanical Engineering, University of California at Santa Barbara, Santa Barbara, CA 93106, USA

[3]Rheinisch-Westfaelische Technische Hochschule Aachen, D-52056 Aachen, Germany

Direct numerical simulations of the variable density and viscosity Navier–Stokes equations are employed, in order to explore three-dimensional effects within miscible displacements in horizontal Hele-Shaw cells. These simulations identify a number of mechanisms concerning the interaction of viscous fingering with a spanwise Rayleigh–Taylor instability. The dominant wavelength of the Rayleigh–Taylor instability along the upper, gravitationally unstable side of the interface generally is shorter than that of the fingering instability. This results in the formation of plumes of the more viscous resident fluid not only in between neighbouring viscous fingers, but also along the centre of fingers, thereby destroying their shoulders and splitting them longitudinally. The streamwise vorticity dipoles forming as a result of the spanwise Rayleigh–Taylor instability place viscous resident fluid in between regions of less viscous, injected fluid, thereby resulting in the formation of gapwise vorticity via the traditional, gap-averaged viscous fingering mechanism. This leads to a strong spatial correlation of both vorticity components. For stronger density contrasts, the streamwise vorticity component increases, while the gapwise component is reduced, thus indicating a transition from viscously dominated to gravitationally dominated displacements. Gap-averaged, time-dependent concentration profiles show that variable density displacement fronts propagate more slowly than their constant density counterparts. This indicates that the gravitational mixing results in a more complete expulsion of the resident fluid from the Hele-Shaw cell. This observation may be of interest in the context of enhanced oil recovery or carbon sequestration applications.

Key words: buoyancy-driven instability, fingering instability, Hele-Shaw flows

1. Introduction

Hele-Shaw displacements have long served as models for corresponding porous media flows, such as those encountered in enhanced oil recovery applications (Homsy 1987). At the same time, Hele-Shaw flows have also been of interest within

† Email address for correspondence: meiburg@engineering.ucsb.edu

the more fundamental context of pattern formation (Maxworthy 1987). Traditionally, most efforts to model Hele-Shaw flows theoretically or computationally have been two-dimensional in nature, based on Darcy's law or its modifications (e.g. Saffman & Taylor 1958; McLean & Saffman 1981; Meiburg & Homsy 1988).

For immiscible displacements, analytical approaches based on perturbation theory have allowed us to gain some insight into the role of three-dimensional effects in the vicinity of the interface (Park & Homsy 1984). For miscible displacements, on the other hand, it has been more difficult to make progress in this regard, due to the non-local effects of diffusion and dispersion (Taylor 1953; Petitjeans *et al.* 1999). The last decade, however, has seen progress in terms of fully three-dimensional treatments of miscible Hele-Shaw flows based on the Stokes or Navier–Stokes equations, both in terms of linear stability analyses and most recently also with regard to nonlinear simulations. The Stokes-based linear stability analysis by Graf, Meiburg & Härtel (2002) was able to reproduce experimentally measured dispersion relations (Fernandez *et al.* 2002) for miscible Rayleigh–Taylor instabilities in vertical Hele-Shaw cells across several orders of magnitude in the Rayleigh number, whereas an equivalent Darcy-based analysis gave approximately valid results only for small Rayleigh numbers. Further comparisons between theoretical models and lattice-Boltzmann simulations for this type of instability are provided by Martin, Rakotomalala & Salin (2002). These Stokes-based linear stability results were subsequently extended to variable density and viscosity displacements in vertical Hele-Shaw cells (Goyal & Meiburg 2004; Goyal, Pichler & Meiburg 2007), cf. also the corresponding experiments by Lajeunesse *et al.* (1997, 1999, 2001), and to constant density, variable viscosity displacements in horizontal cells (Goyal & Meiburg 2006).

The effectiveness of the Hele-Shaw model has also been examined for shear flow instabilities. Gondret & Rabaud (1997) used an Euler–Darcy equation to describe Kelvin–Helmholtz instabilities in Hele-Shaw cells, while Plouraboué & Hinch (2002) improved the linear stability results by basing their analysis on the Navier–Stokes equations.

Very recent nonlinear, three-dimensional simulations of miscible Hele-Shaw displacements by Oliveira & Meiburg (2011) revealed a novel inner splitting mechanism of fully developed fingers, which is in contrast to the more familiar tip-splitting mechanism observed by other authors (e.g. Tan & Homsy 1988). Oliveira & Meiburg (2011) revisited the classical flow visualization images of Wooding (1969) and found evidence of such inner splitting events in those experiments. This inner splitting mechanism owes its existence to a quadrupole streamwise vorticity structure along the length of the finger, which bisects the finger by transporting resident fluid from the walls of the Hele-Shaw cell to the centre. Clearly, such flow structures are three-dimensional in nature, and they cannot be obtained based on two-dimensional, gap-averaged approaches.

Hallez & Magnaudet (2008) perform two- and three-dimensional Navier–Stokes simulations to investigate gravitational mixing of two interpenetrating miscible fluids placed in a tilted tube or channel. They show that differences between the two-dimensional and three-dimensional geometries are associated with the dynamics of the vorticity field. This configuration has been studied experimentally by Séon, Hulin & Salin (2005), Séon *et al.* (2006, 2007).

The goal of the present investigation then is to investigate the role of gravity when such miscible displacements are carried out for variable density fluids in horizontal Hele-Shaw cells. Such flows are substantially more complex than their constant
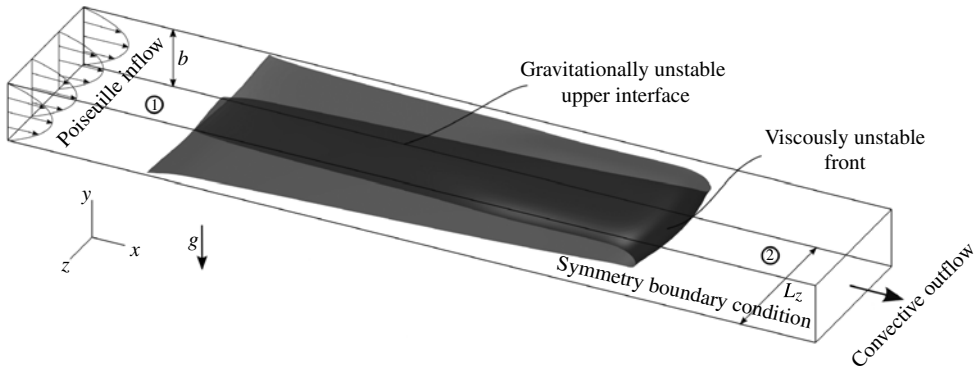
FIGURE 1. Schematic figure showing the problem geometry: injected fluid 1 (μ_1, ρ_1, $c = 0$) displaces resident fluid 2 ($\mu_2 > \mu_1$, $\rho_2 > \rho_1$, $c = 1$) in the positive *x*-direction, driven by Poiseuille inflow. Gravity acts in the negative *y*-direction. Solid walls form the top and bottom boundaries, while symmetry conditions are assumed at the *z*-boundaries. The grey surface denotes the $c = 0.5$ concentration contour, which can be considered a representation of the miscible interface.

density counterparts, as they combine elements of viscously unstable displacements with aspects of gravity currents (Simpson 1997; Hartel, Meiburg & Necker 2000), cf. also related recent experiments in slightly inclined channels by Taghavi *et al.* (2010, 2011*a*,*b*). A linear stability analysis by Talon, Goyal & Meiburg (2013) has been carried out in parallel to the present, nonlinear investigation and is presented separately in part 1 of this investigation. It demonstrates that the fingering instability can be modified substantially by the effects of gravity, while novel, gravitationally driven instabilities can appear at the predominantly horizontal interfaces between the layer of resident fluid left behind on the wall and the injected fluid propagating along the centre of the apparatus. Our interest in the present part 2 of this investigation will focus on the nonlinear evolution of these instability mechanisms.

Towards this end, we first compute quasisteady two-dimensional base states, which are subsequently disturbed along the spanwise direction in order to trigger viscous fingering and Rayleigh–Taylor instabilities. Section 2 introduces the physical problem and formulates the governing equations, whose solution is subsequently described in §3. Validation results are provided in §4 in terms of the two-dimensional base state properties and the early growth rates of their three-dimensional perturbations. Section 5 focuses on the results of the investigation, first for the two-dimensional base states, and subsequently for the fully three-dimensional displacements evolving from these. In particular, we will identify and quantify novel mechanisms governing such flows, and analyse them in terms of their vorticity dynamics. Finally, §6 presents a summary of the findings, along with the main conclusions.

2. Physical problem

We consider a horizontal Hele-Shaw cell of gap width *b*, in which fluid 1 displaces fluid 2, with which it is fully miscible, cf. figure 1. The fluids have different viscosities ($\mu_1 < \mu_2$) as well as different densities ($\rho_1 < \rho_2$). As a result of the unfavourable viscosity ratio, we expect the displacement front to give rise to a fingering instability.

Furthermore, there is the potential for additional gravitational instabilities to develop, for example along the upper interface of the front, where denser resident fluid is situated above lighter injected fluid.

2.1. *Governing equations*

Assuming incompressible flow, we employ as our governing equations for miscible displacements the transient three-dimensional Navier–Stokes equations in the Boussinesq approximation with variable viscosity, coupled to a convection–diffusion equation for the concentration field. In non-dimensional form, they read

$$\frac{\partial u_i}{\partial x_i} = 0, \tag{2.1}$$

$$\frac{\partial u_i}{\partial t} + u_j \frac{\partial u_i}{\partial x_j} = \frac{1}{Re} \left[\frac{\partial}{\partial x_j} \mu \left(\frac{\partial u_i}{\partial x_j} + \frac{\partial u_j}{\partial x_i} \right) - \frac{\partial p}{\partial x_i} \right] - Fc\delta_{i2}, \tag{2.2}$$

$$\frac{\partial c}{\partial t} + u_j \frac{\partial c}{\partial x_j} = \frac{1}{Pe} \frac{\partial}{\partial x_j} \frac{\partial c}{\partial x_j}, \tag{2.3}$$

where u_i indicates the velocity component in the spatial direction x_i, c denotes the concentration of the resident fluid, D the (constant) diffusion coefficient and p the pressure. Here δ_{i2} represents the unit vector in the $+y$-direction. As characteristic scales we employ the length $l^* = b$, time $t^* = b/U$, where U is the gap-averaged inflow velocity, and pressure $p^* = \mu_2 U/b$, along with the smaller density $\rho^* = \rho_1$ and larger viscosity $\mu^* = \mu_2$. In this way, we obtain dimensionless parameters in the form of a Reynolds number $Re = Ub/\nu_2$, gravity parameter $F = \Delta\rho gb/\rho_1 U^2$ and Péclet number $Pe = Ub/D$. Note that the non-dimensionalization of Re is different from that employed in Oliveira & Meiburg (2011), who analysed the neutrally buoyant case. They used the smaller viscosity ν_1 to define the Reynolds number Re'. When comparing with these results, the conversion ratio of Re numbers is therefore $Re' = e^R \cdot Re$, where $R = \ln \mu_2/\mu_1$.

We assume that density is a linear function of the concentration

$$\rho(c) = \rho_1 + c \cdot \Delta\rho, \quad \Delta\rho = \rho_2 - \rho_1, \tag{2.4}$$

while viscosity varies with concentration according to

$$\mu(c) = \mu_2 e^{R \cdot (c-1)}. \tag{2.5}$$

Despite being much simpler to implement, this exponential dependence returns similar results as the quarter power mixing rule frequently used by petroleum engineers (Vanaparthy & Meiburg 2008). Based on the observation by those authors that a concentration-dependent diffusion coefficient has a very small influence on such front properties as their velocity or thickness, we employ a constant diffusion coefficient throughout.

We closely follow Oliveira & Meiburg (2011) and Oliveira (2012) regarding boundary and initial conditions and provide only a summary here. For the velocity field, we impose no-slip conditions at the top and bottom walls, symmetric boundary conditions at the spanwise boundaries and a Poiseuille profile at the streamwise inflow boundary. At the streamwise end of the domain, convective outflow conditions are implemented. The concentration field satisfies an error function across the streamwise
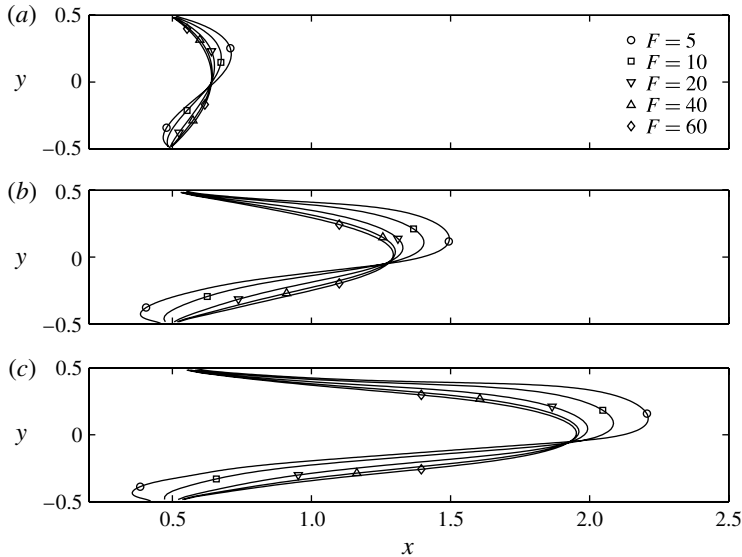
FIGURE 2. Early evolution of the $c = 0.5$ contour for the two-dimensional base states corresponding to the indicated values of F, and times $t = 0.1, 0.5$ and 0.9, $R = 2.0$, $Re = e^{-2.0}$ and $Pe = 2000$.

direction

$$c(x, t = 0) = \frac{1}{2} \left(1 + \mathrm{erf} \left(\frac{x - 0.5}{0.1} \right) \right). \tag{2.6}$$

Beginning at time $t = 0$, the prescribed Poiseuille flow results in the immediate deformation of the initial concentration profile and in the emergence of a two-dimensional base state in the form of a displacement front that propagates in the x-direction along the interior of the cell, see figure 2.

Similarly to the constant density case, after a transient period the front of this finger assumes a quasisteady shape in a moving reference frame. Consistent with the Stokes flow observations by Goyal & Meiburg (2006) for the constant density case, this quasisteady shape does not depend on the thickness of the initial error function profile, so that we keep its value at 0.1 for all simulations. Regarding the negligible influence of the initial interface thickness, cf. also the recent experiments by Aubertin *et al.* (2009).

2.2. *Disturbing the two-dimensional base state*

In order to trigger a fully three-dimensional evolution, we disturb the quasisteady, two-dimensional base state with a small amplitude, sinusoidal perturbation in the spanwise z-direction at time $t = 2.0$. This perturbation effectively displaces the interface either in the streamwise or in the vertical direction, as will be explained in detail below.

For validation purposes, we would like to compare the growth rates of these perturbations with results from the accompanying linear stability analysis of Talon *et al.* (2013). As pointed out by those authors, two different types of dominant perturbations can evolve, namely a viscously dominated mode along the front, and a

Rayleigh–Taylor mode along the top interface. They presented separate sets of linear growth rate results for each of these modes.

Within the fully nonlinear simulations, we attempt to trigger these different modes by imposing one of the two following types of perturbations, which instantaneously shift the concentration field at time $t = t_{dist}$ according to

$$c_g(x, y, z) \rightarrow c_g\left(x, y + A\cos\left(\frac{2\pi}{\lambda}z\right), z\right), \qquad (2.7a)$$

$$c_v(x, y, z) \rightarrow c_v\left(x + A\cos\left(\frac{2\pi}{\lambda}z\right), y, z\right). \qquad (2.7b)$$

Here A denotes the amplitude, typically $\mathcal{O}(10^{-3})$, and λ the wavelength, which is chosen to be the one of maximum growth, as predicted by Talon *et al.* (2013) as a function of (F, R, Pe). The perturbation c_g displaces the interface alternatingly upwards and downwards in the spanwise direction, which primarily triggers the Rayleigh–Taylor instability mode along the upper interface. Conversely, c_v displaces the interface in the upstream and downstream directions, which results in the preferential evolution of viscous fingering along the displacement front. In this way we are able to obtain approximate growth rates separately for both of the dominant instability modes from the fully nonlinear simulations, which can then be compared with the respective linear stability results of Talon *et al.* (2013).

3. Numerical implementation

The numerical solution of the governing equations largely follows the approach described by Oliveira & Meiburg (2011) and by Oliveira (2012), so that we provide only a brief summary here.

The governing equations are solved directly on a staggered grid. They are discretized spatially by second-order central differences, with a fifth-order WENO scheme (Jiang & Peng 2000) employed for the derivatives of convective terms, due to the presence of steep concentration gradients. The temporal integration is performed using a fractional step method following Kim & Moin (1985). In the past, this method was successfully combined with a three-step hybrid Runge–Kutta/Crank–Nicolson (RK/CN) time integration scheme, for which convective and diffusive terms are treated separately, using the explicit RK scheme for the convective and the implicit CN scheme for the viscous terms, respectively, see Rai & Moin (1991). By explicitly including the pressure gradient into the projection step, we solve the Poisson equation using cosine transforms for a scalar related to pressure and make the projection scheme more accurate.

3.1. *Adaptive domain size*

In order to improve on the efficiency of the simulation approach by Oliveira & Meiburg (2011), we let the size of the computational domain grow with time. This allows us to employ relatively small domain sizes during the early stages of the simulation, so that we do not spend a large amount of numerical effort on those sections far downstream of the front where the flow is essentially of Poiseuille type. Making use of the existing parallel implementation the adaptive domain size algorithm interrupts the simulation well before the displacement front reaches the outflow boundary. The domain size is then increased by adding a new subdomain initially containing Poiseuille flow. In this fashion, the average domain size over the duration of the entire simulation is approximately halved.
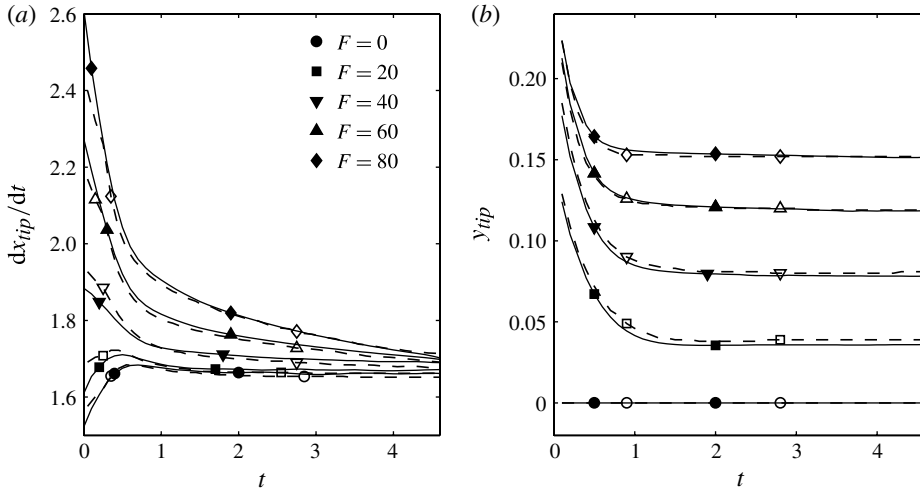
FIGURE 3. Velocity of the front dx_{tip}/dt and front elevation y_{tip} (—) as a function of time for various F, $R = 2.5$, $Pe = 2000$ and $Re = e^{-2.5}$. The Stokes flow results of Talon *et al.* (2013) are shown for comparison (- - -).

4. Validation

4.1. *Front properties*

A first validation step focuses on the properties of the two-dimensional base states. We remark that the two-dimensional simulations presented in the current work were carried out with the three-dimensional code, by keeping only three grid points in the spanwise direction. Those, when combined with the ghost nodes, provide the minimum stencil necessary for the WENO discretization. The finger tip $\{x_{tip}, y_{tip}\}$ is defined as the rightmost point of the $c = 0.5$ contour, which is accurately determined by means of two-dimensional spline interpolation between the grid points. Bearing in mind that for $F \neq 0$ the flow is not symmetric in the y-direction, we always found a unique value for y_{tip}. For a small value of $Re = e^{-2.5}$, figure 3 shows the velocity of the tip dx_{tip}/dt along with the vertical elevation of the tip y_{tip} for various F, during the early stages of the flow as the quasisteady base state develops. The Stokes flow results reported by Talon *et al.* (2013) are given for comparison. We remark that we generated a Navier–Stokes simulation code instead of a Stokes flow code, since we eventually plan to explore the effects of inertia at higher Reynolds numbers. However, in the present analysis we kept Re small enough so that inertial effects are negligible. This is confirmed by the good agreement with the results of Talon *et al.* (2013), which are based on the Stokes equations. Analogous front velocity results were obtained for the dependence on R and Pe, for various F-values. The errors for the velocities and the front elevations generally are of $\mathcal{O}(10^{-2})$ or less, for all F and times. This represents satisfactory agreement, when taking into account that an entirely different numerical environment was used, and that the present Navier–Stokes results are compared with the Stokes values of Talon *et al.* (2013).

4.2. *Instability growth rates*

A subsequent second validation step was performed by evaluating the linear growth rates σ during the early three-dimensional stages, for both the viscous fingering

F	R	σ_T^v	$\sigma_{w_{max}}^v$	ϵ_w (%)	$\sigma_{\Omega_x}^v$	ϵ_Ω (%)
60	3.0	0.935	0.730	-21.9		
60	2.5	0.698	0.562	-24.6	0.646	-7.5
60	2.0	0.418	0.340	-18.7	0.418	-10.1
40	3.0	0.865	0.782	-9.6		
40	2.5	0.652	0.565	-13.3		
40	2.0	0.407	0.374	-8.1	0.371	-8.9
20	3.0	0.788	0.813	3.2		
20	2.5	0.614				
20	2.0	0.392	0.371	-5.4	0.375	-4.3

TABLE 1. Computationally evaluated growth rates $\sigma_{w_{max}}^v$ of the viscously most unstable mode, determined from the maximum spanwise velocity w_{max} near the finger tip and $\sigma_{\Omega_x}^v$ as determined from the maximum streamwise vorticity in the entire domain, for $Pe = 2000$ and $Re = e^{-R}$. The linear stability analysis results σ_T^v of Talon *et al.* (2013) are given for comparison, with ϵ indicating the relative error.

F	R	σ_T^g	$\sigma_{w_{max}}^g$	ϵ_w (%)
60	3.0	1.723	1.709	-0.8
60	2.5	1.374	1.468	6.8
60	2.0	1.106	1.076	-2.7
40	3.0	1.202	1.236	2.8
40	2.5	0.988	0.959	-2.9
40	2.0	0.827	0.828	0.1
20	3.0	0.651	0.664	2.0
20	2.5	0.554	0.539	-2.7
20	2.0	0.488	0.456	-6.6

TABLE 2. Computationally evaluated growth rates $\sigma_{w_{max}}^g$ of the gravitationally most unstable mode, determined from the maximum spanwise velocity w_{max} at the upper $c = 0.5$ concentration contour of the finger, compared with the linear stability analysis results σ_T^g of Talon *et al.* (2013).

instability at the displacement front and the gravitational instability at the upper interface. To obtain the growth rate, we recorded the maximum spanwise velocity as a function of time throughout the simulation, either in a sufficiently large control volume around the displacement front, or along the upper $c = 0.5$ contour. As an alternative, we also recorded the maximum streamwise vorticity within the entire domain. Continuous loci of the maxima were found, and exponential growth could be observed over a moderately long time interval (typically 5–10 units of time) for most values of F and R. Where unique values were found, the data so obtained are compared with the linear stability results of Talon *et al.* (2013) in table 1 for the viscous instability and in table 2 for the gravitational instability. Typical errors for the growth rate of the viscous instability range from $\mathcal{O}(5\%)$ for moderate values of the gravity parameter $F \approx 20$, to $\mathcal{O}(20\%)$ for $F = 60$. For the gravitational instability, we see good agreement across the entire range of F-values, with errors of $\mathcal{O}(5\%)$.

5. Results

In the following, we focus on the influence of F on the nonlinear dynamics and pattern formation of miscible fingering in horizontal displacements. For this purpose, we hold the remaining governing parameters constant at the values $M = 2$, $Re = e^{-2}$ and $Pe = 2000$. The F-value ranges from $F = 0$ to a maximum of $F = 60$.

5.1. *Two-dimensional base state*

5.1.1. *Long-term evolution of front velocity and elevation*

As we saw earlier in figures 2 and 3, larger gravity numbers F result in increasingly elevated quasisteady displacement fronts, which are associated with more pronounced interface curvature and an initially faster streamwise front velocity. Beyond the quasisteady state shown in figure 3, however, the displacement front gradually slows down and moves towards the centreline of the channel. Interestingly, for long times the early trend reverses, in that larger F-values result in slower displacement fronts, cf. figure 4(*b*), which shows the long-term behaviour of the front velocity $\mathrm{d}x_{tip}/\mathrm{d}t$. For comparison, the velocity at the front $u_{tip} = u(x_{tip}, y_{tip})$ is shown in figure 4(*c*). As discussed by Oliveira & Meiburg (2011), whenever $\mathrm{d}x_{tip}/\mathrm{d}t$ is larger (smaller) than u_{tip}, fluid particles will cross the interface from right (left) to left (right).

In the neutrally buoyant case the maximum streamwise fluid velocity is found at the midgap position. Owing to the loss of vertical symmetry due to density difference effects for non-zero F-values, the location of the u_{tip}-maximum across the gap can now lie above $y = y_{tip}$. Furthermore, we observe that beyond $t = 30$ the tip elevation y_{tip} for the case $F = 60$ abruptly rises, with smaller F-values showing a similar trend at somewhat later times. We now proceed to discuss the mechanisms governing this unexpected behaviour.

5.1.2. *Two-dimensional pinch-off mechanisms*

We now describe two phenomena that can affect the two-dimensional evolution of the displacement front for long times. The first is shown in figure 5 for a constant density displacement. In these figures, we recognize that the tip itself still contains some relatively undiluted less viscous fluid. However, immediately behind the tip, the concentration contours from opposite sides of the finger approach each other and successively pinch off. We also note that there is substantial vorticity present along the entire length of the finger. However, this spanwise vorticity has a predominantly layered structure, so that it mostly promotes the transport of undiluted injected fluid in the x-direction, towards the front. The small vorticity peak within the finger tip near $x = 80$ augments this transport of injected fluid into the tip of the front. At the same time, it also tends to favour the transport of resident fluid from the walls towards the centre immediately behind the finger tip. We hence term this phenomenon 'dispersive pinch-off'.

Figure 6 displays the value of the vorticity maximum within the vortex immediately behind the tip, as a function of time. It demonstrates that the vorticity transiently grows and reaches a maximum soon after the base state forms, but then declines monotonically with time. Furthermore, as gravitational effects become important, the strength of this vortex increases.

Figure 7 shows a fundamentally different pinch-off mechanism, which we term 'gravitational pinch-off'. It occurs much farther behind the tip than the dispersive pinch-off. We observe the sinking of a large amount of heavy fluid over an extended x-interval, which effectively separates the tip of the displacement front from the bulk of the finger. The sinking of heavy fluid from the top wall allows the separated
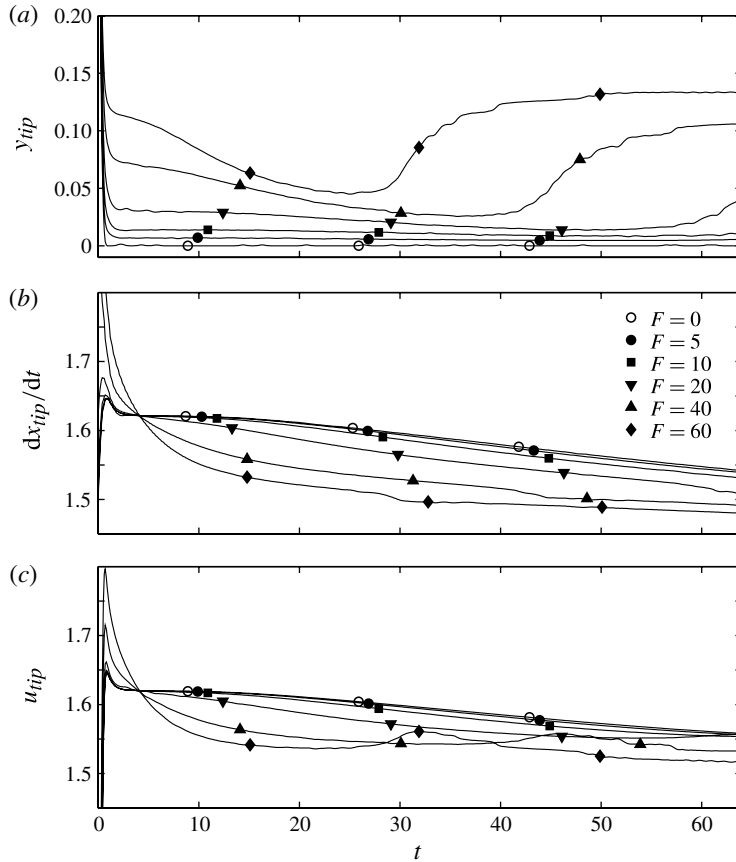
FIGURE 4. Long-time behaviour of two-dimensional base flows: y_{tip}, $\mathrm{d}x_{tip}/\mathrm{d}t$ and u_{tip} for various F. The raw data are smoothed by taking mean values over a moving window of 0.5 units of time. Here $Pe = 2000$, $R = 2.0$ and $Re = e^{-2.0}$. Beyond $t > 5$ larger F-values are seen to result in slower displacement fronts. Beyond $t > 30$, the tip elevation of the front abruptly rises for $F = 60$, as explained in the text. (b,c) Comparison of the velocity of the tip ($\mathrm{d}x_{tip}/\mathrm{d}t$) and the fluid velocity *at* the tip (u_{tip}), respectively. Fluid particles cross the interface from right (left) to left (right) if $\mathrm{d}x_{tip}/\mathrm{d}t$ is larger (smaller) than u_{tip}.

finger tip to rise into the space vacated by this heavy fluid, which explains the abrupt increase in the tip elevation that we saw in figure 4. Simultaneously, the tip slows down, as it is effectively cut off from the continued supply of fresh injected fluid, again in agreement with the front velocity data shown in figure 4.

Figure 8 summarizes the findings on dispersive and gravitational pinch-off. It shows the times until individual contour levels undergo pinch-off, as function of the gravitational parameter F. The process by which the lower concentration levels split shows little dependence on F, indicating that it is dispersively dominated. By comparison, gravitational effects have only a weak influence. However, we notice a slight delay in pinch-off time for larger F-values, which is related to the increasing strength of the vortex immediately behind the front, as seen in figure 6. The change in slope near $c \approx 0.35$ for $F = 60$ signals the transition from dispersive to gravitational pinch-off. Within the simulation times investigated here, the highest concentration
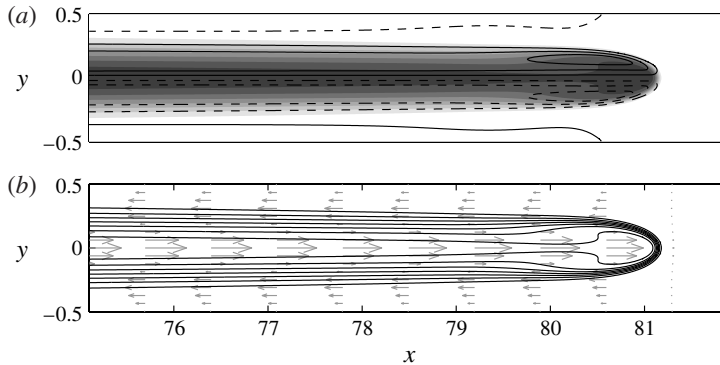
FIGURE 5. Dispersive pinch-off of the concentration contours immediately behind the finger tip. (*a*) Concentration field ($\Delta c = 0.1$) in grey levels and contour lines of vorticity after the base Poiseuille flow has been subtracted out. Positive vorticity is represented by continuous lines and negative vorticity by dashed ones. (*b*) Black contours show the concentration field and grey arrows represent the velocity field, after the base Poiseuille flow has been subtracted out. Time $t = 50$, the parameter values are $F = 0$, $R = 2.0$, $Re = e^{-2.0}$ and $Pe = 2000$. Here, the $c = 0.2$ contour has already pinched off, and the $c = 0.3$ contour is about to pinch off near $x = 80$, cf. also figure 8 for the pinch-off times of the concentration contours.
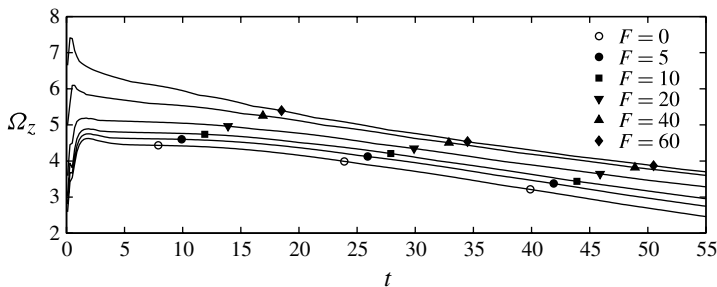
FIGURE 6. Maximum vorticity within the vortex immediately behind and above the tip, as a function of time and for various F. The other parameter values are $R = 2.0$, $Re = e^{-2.0}$ and $Pe = 2000$.

levels did not undergo pinch-off for low values of F, so that we observed gravitational pinch-off only for $F = 60$.

5.2. *Three-dimensional flows*

For three-dimensional flow simulations, we choose the spanwise domain size equal to the wavelength of the most amplified viscous mode. Since the wavelength of the gravitational mode is typically significantly shorter than that of the viscous mode, this domain size will allow for gravitational modes to evolve as well. To trigger the three-dimensional evolution, we introduce at $t = 2$ a disturbance of the viscous type c_v (see (2.7)) with amplitude $A = 0.03$.

5.2.1. *Cavity formation, tip velocity and elevation*

Figure 9 shows a representative case of a three-dimensional flow. We can clearly recognize that the gravitational term has resulted in a loss of the up–down symmetry
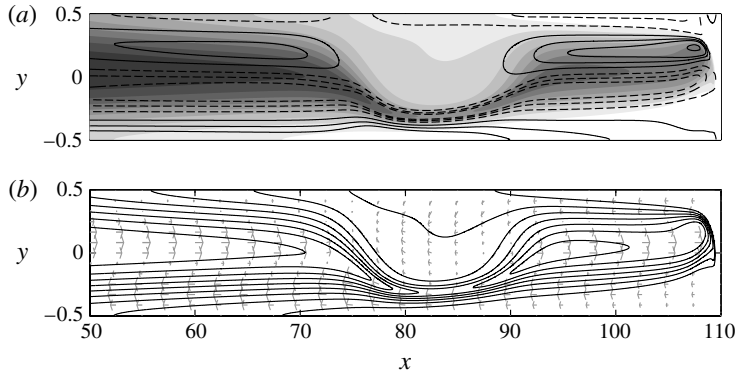
FIGURE 7. Gravitationally dominated pinch-off of the concentration contours far behind the finger tip. (*a*) Grey levels of the concentration field ($\Delta c = 0.1$) and contour lines of vorticity after the base Poiseuille flow has been subtracted out. Positive vorticity is represented by continuous lines, and negative vorticity by dashed ones. (*b*) Concentration contours (black lines) and velocity field after the base Poiseuille flow has been subtracted out. Time $t = 71.0$, the parameter values are $F = 60$, $R = 2.0$, $Re = e^{-2.0}$ and $Pe = 2000$. The $c = 0.4$ contour has already pinched off and the $c = 0.5$ is about to pinch off near $x = 84$, cf. also figure 8 for the pinch-off times.
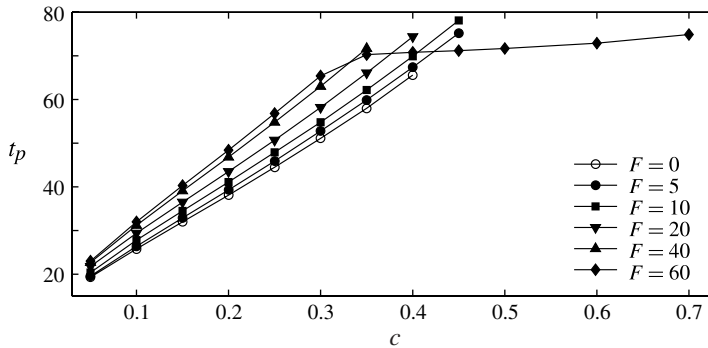
FIGURE 8. Pinch-off times of concentration contours as function of F, for $R = 2.0$, $Re = e^{-2.0}$ and $Pe = 2000$. The lower concentration levels pinch off primarily as a result of dispersive pinching, whereas gravitational effects are responsible for the pinch-off of the larger concentration levels.

about the $y = 0$ plane. While the top surface shows a pronounced, elongated cavity along $z = 0$ in the region $15 < x < 27$, no such cavity exists on the lower surface of the finger, which is gravitationally stable due to the presence of lighter fluid above denser fluid.

The origin of this cavity becomes clear from the $x = const.$ cross-cut shown in figure 10. This figure displays the concentration field (in grey shading) along with a projection of the velocity field onto the $x = const.$ plane. It demonstrates that the cavity formation is associated with a negatively buoyant plume of the denser fluid near $z = 0$, which is propelled downwards by a streamwise vortex dipole and thus bisects the finger lengthwise. This process is a clear manifestation of a Rayleigh–Taylor
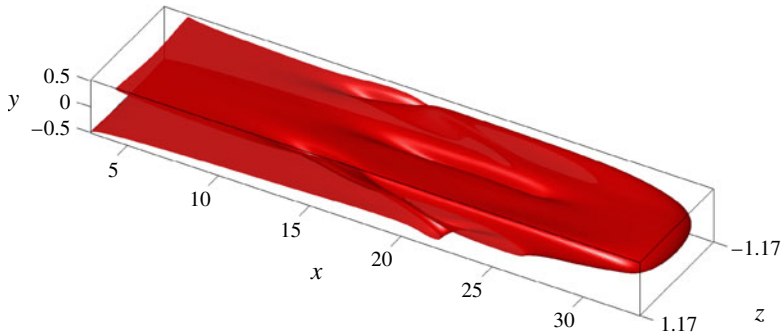
FIGURE 9. (Colour online) Representative three-dimensional flow evolution, for $F = 20$, $R = 2.0$, $Re = e^{-2.0}$ and $Pe = 2000$. Shown is the $c = 0.5$ contour at $t = 20$. A gravitational cavity forms near $z = 0$ in the interval $15 < x < 27$, as a result of heavier resident fluid sinking into the lighter, less viscous finger body.
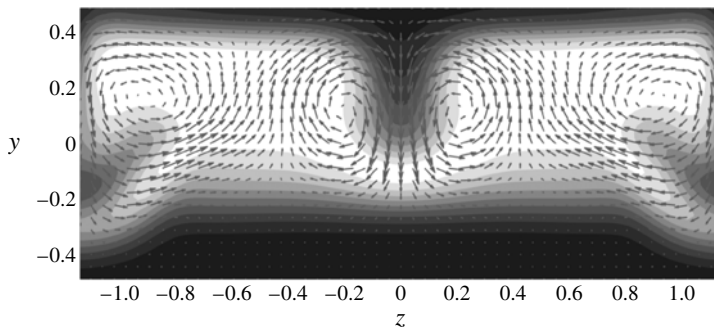

FIGURE 10. Cross-sectional view of the concentration and velocity fields at $x = 22$, for the flow shown in figure 9. The inner cavity forms as a negatively buoyant plume sinks near $z = 0$, propelled by a vortex dipole.

instability in the spanwise direction, as investigated in the linear stability analysis of Talon *et al.* (2013). Those authors show that a spanwise Rayleigh–Taylor instability along the upper side of a displacement front typically has a most amplified wavelength that is several times shorter than the dominant wavelength of the viscous fingering instability. Hence, we expect to see more than one wavelength of the Rayleigh–Taylor instability within one viscous fingering wavelength. This is consistent with the present observation of a Rayleigh–Taylor instability wavelength half as long as the viscous fingering instability wavelength, so that negatively buoyant plumes form at $z = -L_z/2$, $z = 0$ and $z = L_z/2$. Note that the gravitational splitting is a three-dimensional effect associated with the spanwise direction, as opposed to the gravitational pinch-off described earlier, which occurs even in the two-dimensional base flow.

We remark that the present, gravitational splitting is fundamentally different from the inner splitting described by Oliveira & Meiburg (2011) for constant density displacements. In those flows, a pronounced quadrupole streamwise vorticity structure forms which convects resident fluid from the walls to the centre in a symmetric fashion, thereby resulting in a splitting event. When gravitational forces become important, this streamwise vorticity quadrupole gives way to the dipole structure near
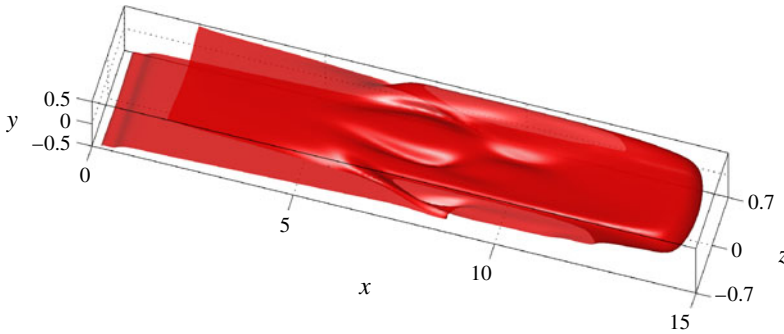
FIGURE 11. (Colour online) Three-dimensional perspective showing the $c = 0.5$ concentration contour for $F = 60$, $R = 2.5$, $Re = e^{-2.5}$ and $Pe = 2000$ at time $t = 8.1$. Note that two additional cavities appear behind the cavity being formed near $x = 10$.

the centre of the cell shown in figure 10, which leads to an asymmetric splitting. It appears possible that for flows such as that shown in figure 9 these two splitting mechanisms may amplify each other, since the gravitational dipole structure is of the same sign and in approximately the same location as one half of the quadrupole structure in the constant density displacement. However, for other values of F it is possible that the ratio of the dominant Rayleigh–Taylor and viscous fingering instability wavelengths will be such that not one, but multiple cavities might form on the upper side of the front (see figure 11). For those cases, the amplification of the gravitational splitting by the constant density inner splitting becomes dependent on the streamwise position and the number of gravitational cavities.

We emphasize that for the flows reported in this section, the imposed perturbation primarily triggers the viscous instability. Early on, the viscous mode dominates and establishes the finger, and it allows for vertical fluid transport in the gaps between neighbouring fingers. The gravitational mode then develops on top of that, and since there is already vertical fluid transport occurring in the gap between neighbouring fingers, those wavenumbers of the gravitational mode that are a multiple of the viscous mode are preferred.

The gravitational splitting mechanism provides the dense fluid above the viscous finger with a more direct path to escape from the near-wall region than having to move laterally all of the way around the sides of the viscous finger. As the dense fluid from above the finger moves downward through the cavity, the buoyant viscous finger is able to rise towards the top wall into the space vacated by the dense fluid. Figure 12(*a*) shows the resulting sudden and rapid increase of the front elevation y_{tip} for different values of F. As expected, larger values of F result in earlier cavity formation, so that the dense fluid above the finger can escape more rapidly and the front rises earlier. From the front velocity data shown in figure 12(*b*), we see that the front generally slows down as it rises and approaches the wall, which enhances the overall displacement efficiency.

5.2.2. *Shoulder deformation*

We define the shoulder of the finger as the region near the lateral symmetry boundaries $z = \pm L_z/2$ where neighbouring fingers initially are connected, i.e. where initially $c < 0.5$. As we saw above in figure 10, negatively buoyant plumes of the heavier, more viscous fluid also form in these shoulder regions. In fact, they form
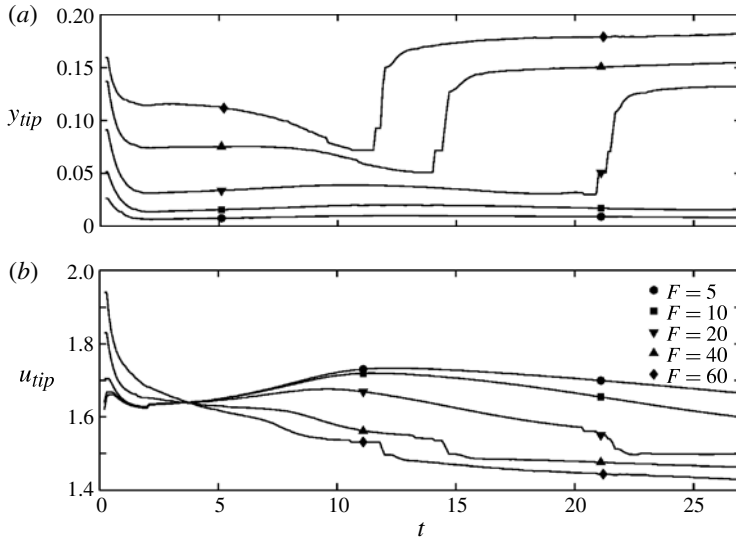
FIGURE 12. Tip elevation y_{tip} and velocity at the front u_{tip} as functions of F, for $R = 2.0$, $Re = e^{-2.0}$ and $Pe = 2000$. The tip elevation is seen to rise abruptly, as a result of the gravitational cavity formation. A comparison with the two-dimensional results of figure 4 shows that the finger tip moves faster than the corresponding two-dimensional displacement front.

more rapidly at the shoulders of the fingers than near $z = 0$ because at the shoulder the viscous fingering instability also leads to a thinning of the displacement front, so that the two instabilities locally amplify each other. The three-dimensional view in figure 13, along with the cross-cuts shown in figure 14(*a,b*) indicate that these sinking plumes can destroy the shoulders, i.e. sever the $c = 0.5$ contour at the lateral domain boundaries $z = \pm L_z/2$, thereby effectively disconnecting neighbouring fingers. We recognize that the fingers are still connected at $t = 7$, while they have become disconnected at the lateral boundaries in the interval $9 < x < 11$ at $t = 7.5$.

In fact, it appears possible for the negatively buoyant plumes that form the inner cavities and destroy the shoulders to generate finger-like flow patterns even in the absence of an unfavourable viscosity contrast. If the two fluids have equal viscosities, the two-dimensional base state will consist of a Poiseuille flow modified by buoyancy forces. The spanwise Rayleigh–Taylor instability will then generate negatively buoyant plumes that cut through this two-dimensional displacement front at regular spanwise intervals, thereby dividing it up into periodic finger-like flow structures.

We note that by destroying the shoulder connecting neighbouring fingers, the gravitational instability can drastically increase the effective length of individual fingers. This hints at a very interesting interplay between the gapwise vorticity that creates the viscous fingers in the first place and the streamwise vorticity associated with the sinking plumes that makes them longer by disconnecting them from their neighbours at the root. Properties of the vorticity field will be discussed in more detail below.

Occasionally, the opposite effect can also occur and two disconnected fingers can become reconnected across the lateral symmetry boundaries some distance downstream of the shoulder, as a result of spanwise fluid motion within the fingers. During this
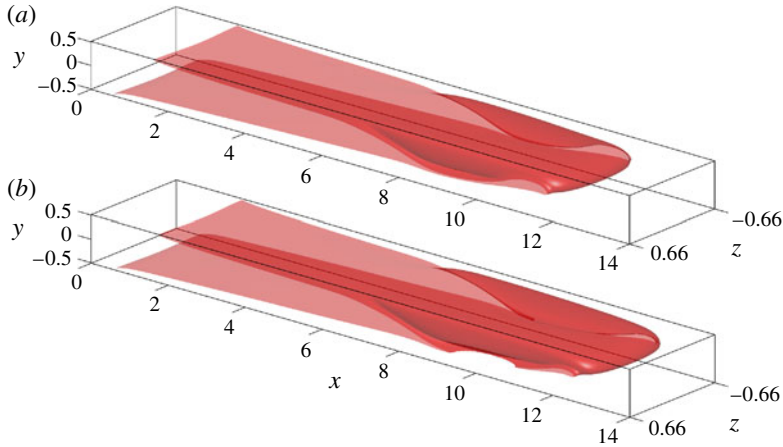
FIGURE 13. (Colour online) Shoulder destruction by negatively buoyant plumes of the dense resident fluid near the lateral domain boundaries $z = \pm L_z/2$: (*a*) $t = 7.0$, neighbouring fingers are still connected at the domain boundary; (*b*) $t = 7.5$, neighbouring fingers have become disconnected by the sinking plume in the region $9 < x < 11$. Shown are the $c = 0.5$ contours for $F = 60$, $R = 2.0$, $Re = e^{-2.0}$ and $Pe = 2000$.
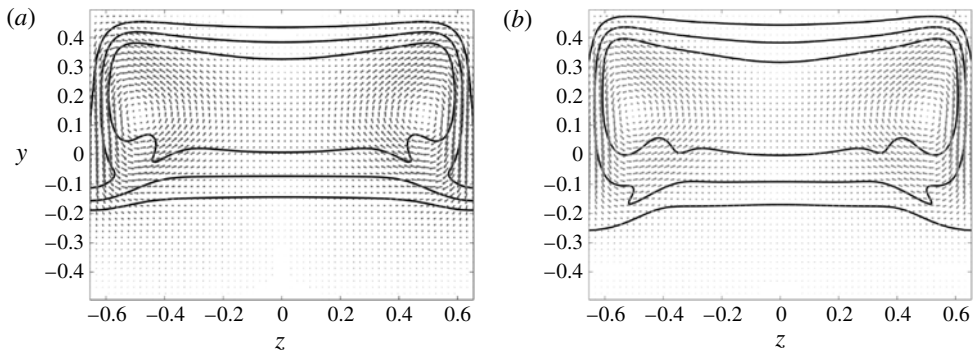

FIGURE 14. Concentration contours $c = 0.1$, 0.5 and 0.9 and the (v, w)-velocity field at $x = 10$, for the flow shown in figure 13: (*a*) $t = 7.0$, the $c = 0.5$ contours are still connected across the lateral symmetry boundaries at $z = \pm L_z/2$; (*b*) $t = 7.5$, the sinking plume of dense fluid has severed the $c = 0.5$ contours at the lateral boundaries, thus effectively disconnecting neighbouring fingers.

process, some of the resident fluid may get trapped in between the original shoulder location and the newly formed connection between the neighbouring fingers. Without providing detailed data, we just remark that such trapping was primarily observed for larger F-values.

5.2.3. *Three-dimensional finger tip deformation*

We now discuss aspects of the three-dimensional finger tip shape and how this is being affected by density differences. To illustrate the substantial influence that gravitational effects can have on the shape of the finger tip, figure 15 shows concentration contours within the planes $y = y_{tip}(F, t)$, for a variety of F-values and
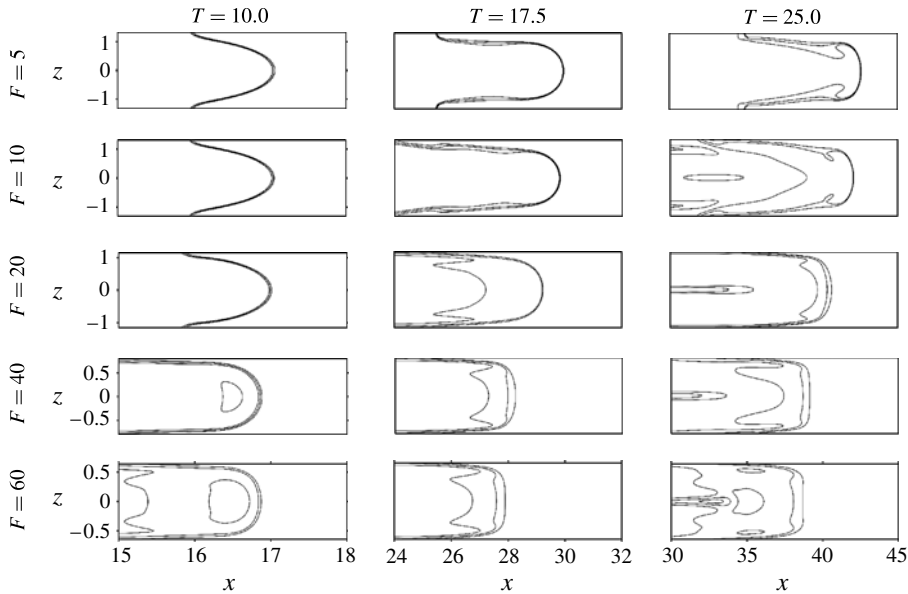
FIGURE 15. Concentration contours $c = 0.1$, 0.3 and 0.5 within the planes $y = y_{tip}(F, t)$ for various F-values and times. The other parameter values are $R = 2.0$, $Pe = 2000$ and $Re = e^{-2.0}$. Purely viscously driven fingers favour a round tip shape, while gravitational effects result in a flatter shape of the finger tip.

different times. While the purely viscous instability tends to form round finger tips, increasing values of F result in blunter, squared off tip shapes. Also note that the tip velocity is reduced substantially for larger F, which indicates an overall higher displacement efficiency. This important global property will be discussed in more detail below, in the context of the time-dependent cross-section averaged concentration profiles.

Figure 16 presents longitudinal cross-cuts of fingers in the symmetry plane $z = 0$, for a variety of F-values and times. Both for small F and large times, as well as for large F and small times, a 'droplet'-like structure can be observed at the very tip of the finger, located on its lower side. However, within the different F-regimes these structures owe their existence to different mechanisms. The droplet seen on the lower side of the finger tip for $F = 5$ at $t = 25$ is a result of the three-dimensional analogue of the dispersive pinch-off described earlier for $F = 0$, cf. figure 5. For the present, small but non-zero F-values this pinch-off has lost its top–bottom symmetry, so that the droplet-like structure appears only on the lower side of the finger tip.

On the other hand, the droplet observed for $F = 60$ at $t = 10$ is a result of gravitational forces, which tend to lift the upstream sections of buoyant finger while the finger tip tends to move down towards the higher velocity region at the centre of the cell. The upward indentation behind the droplet resembles the 'dimple' described by Vanaparthy & Meiburg (2008) in their three-dimensional capillary tube displacement simulations for $F \neq 0$. Those authors speculated that this dimple might be a precursor of a longitudinal splitting along the symmetry plane of the finger, as observed in the experiments of Petitjeans & Maxworthy (1996). However, they could not run their simulations for sufficiently long times to fully describe the subsequent evolution. In the present, Hele-Shaw cell simulations this dimple disappears with time,
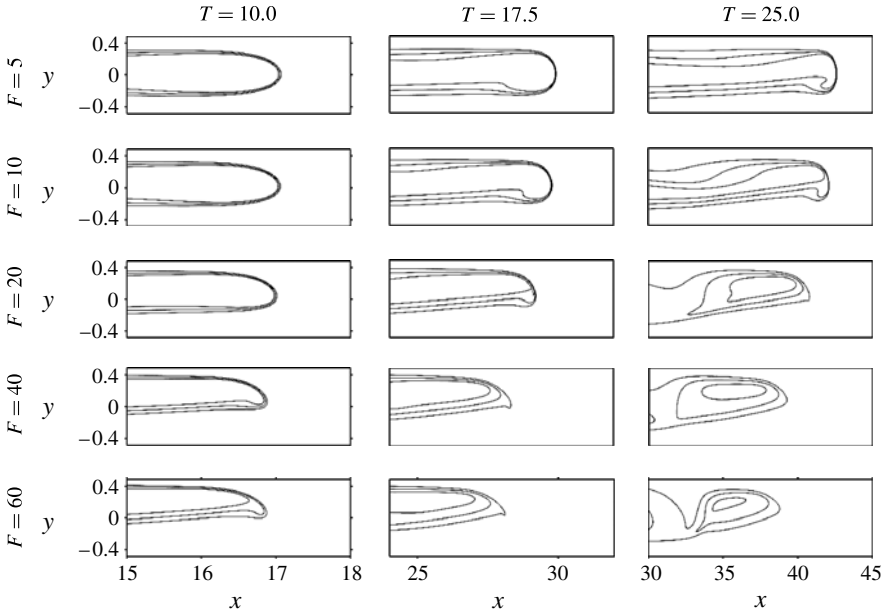
FIGURE 16. Longitudinal cross-cuts of fingers at the symmetry plane $z = 0$, for various F-values and times. The other parameter values are $R = 2.0$, $Re = e^{-2.0}$ and $Pe = 2000$. Shown are the concentration contours $c = 0.1$, 0.3 and 0.5.
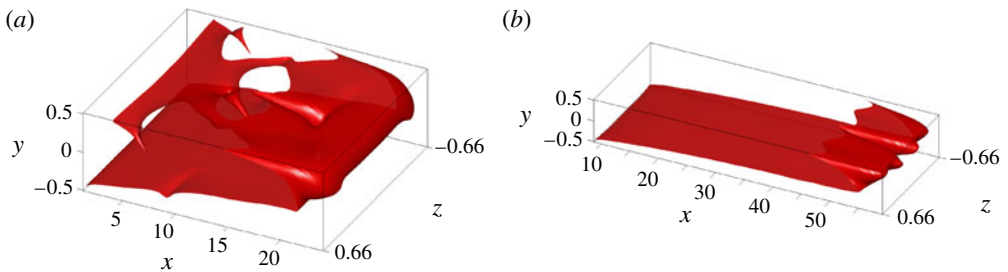

FIGURE 17. (Colour online) Long-time behaviour of the three-dimensional finger for $R = 2.0$, $Pe = 2000$, $Re = e^{-2.0}$ and $F = 60$: (a) $t = 15$, the upper interface being diffused away; (b) $t = 43$, the final quasisteady configuration after the cavity has bisected the tip.

as it is overwhelmed by the formation of a large inner cavity in the $z = 0$ symmetry plane, as shown for $F = 60$ and $t = 25$ and described in detail earlier.

5.2.4. *Long-time behaviour*

As detailed above, for $F = 60$ the shoulder destruction occurs near $t = 7$ and around time $t = 10$ the gravitational cavity starts to develop. Figure 17 shows the $c = 0.5$ contour at later times. By $t = 15$ it has risen close to the top wall and even later it no longer exists near the top wall. By contrast, near the lower wall it still resembles a traditional fingering interface. The cavity has moved downstream and bisected the tip, as shown in figure 17(b) at $t = 43$.
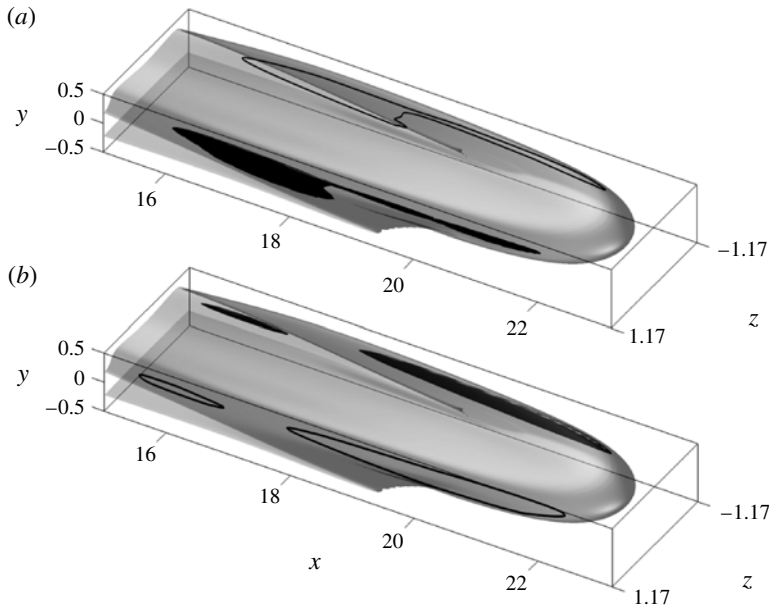
FIGURE 18. Isosurface of concentration $c = 0.5$ (light grey) and vorticity isosurfaces superimposed, for $F = 20$, $R = 2.0$, $Re = e^{-2.0}$ and $Pe = 2000$ at $t = 13.5$: (*a*) streamwise vorticity contours (dark grey $+2.0$, transparent -2.0); (*b*) gapwise vorticity contours (dark grey $+2.25$, transparent -2.25). Note the strong spatial correlation of streamwise and gapwise vorticity, both within the A vortices near $18 < x < 22$ and in the shoulder vortices near $16 < x < 18$.

Interestingly, the two-dimensional shape of figure 7 presents a remarkably different behaviour. After the gravitational pinch-off takes place, the $c = 0.5$ contour remains intact near the upper and lower walls, suggesting that the pinching mechanism could be repeated later on. For three-dimensional dynamics, on the other hand, a second pinch-off would seem unlikely to occur.

5.3. *Vorticity dynamics*

We now discuss properties of the streamwise and gapwise vorticity components obtained by taking the curl of the velocity field. For the case $F = 20$, $R = 2$, $Re = e^{-2.0}$ and $Pe = 2000$, figure 18 shows streamwise and gapwise vorticity contours at the early time $t = 13.5$. The strong spatial correlation of these two vorticity components is striking. The streamwise vorticity dipole closer to the front of the finger, approximately in the interval $18 < x < 22$, which we call A vortices, is associated with the negatively buoyant plume of sinking resident fluid that forms in between neighbouring fingers as a result of the Rayleigh–Taylor instability, as discussed earlier. These plumes place viscous, resident fluid in between neighbouring fingers of less viscous, injected fluid, thereby generating z-gradients in the viscosity. This, in turn, will immediately trigger the production of gapwise vorticity due to the viscous fingering instability mechanism. Hence, streamwise and gapwise vorticity coexists in approximately the same location. The same mechanism is at work further upstream, forming shoulder vortices in the region near $15 < x < 18$. Note that the resulting
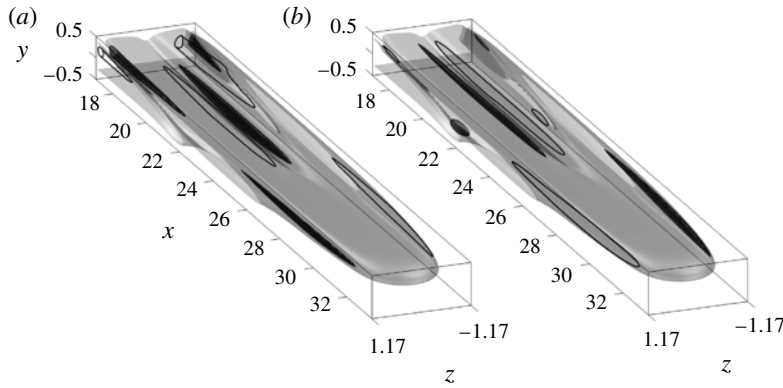
FIGURE 19. Isosurface of concentration $c = 0.5$ (light grey) and vorticity isosurfaces superimposed, for $F = 20$, $R = 2.0$, $Re = e^{-2.0}$, $Pe = 2000$ at $t = 20.0$. Inner vortices clearly visible around cavity for both of the components: (*a*) streamwise vorticity (dark grey $+1.5$, transparent -1.5) and (*b*) gapwise vorticity (dark grey $+1.7$, transparent -1.7). The rear of the A vorticity branch meets the front part of the inner vortices at the location $x \approx 25$.

dipole structure of the vorticity field is fundamentally different from the quadrupole structure observed by Oliveira & Meiburg (2011) for neutrally buoyant displacements.

Above we had seen that the cavity dipole near $z = 0$ forms somewhat later in time than the dipole near the lateral symmetry boundaries $z = \pm L_z/2$. This observation is consistent with figure 19(*a*), which shows that for the same flow as in figure 18 a streamwise cavity dipole has formed by $t = 20$, in the region $19 < x < 25$, which we call inner vorticity. As the cavity forms, viscous resident fluid is again placed in between regions of less viscous injected fluid, so that the viscous fingering mechanism immediately results in the production of gapwise vorticity in approximately the same location, as seen in figure 19(*b*).

Further information on how changes in F affect the flow field is provided by the $x = \text{const.}$ cross-cuts shown in figure 20 ($F = 10$) and figure 21 ($F = 60$). For the lower F-value, we find that as the tip approaches a certain x-location, it pushes the resident fluid radially outwards in a source flow-like fashion that maintains an approximate top–bottom symmetry and resembles the $F = 0$ case analysed by Oliveira & Meiburg (2011). However, while Oliveira & Meiburg (2011) observed a quadrupole streamwise vorticity structure behind the front for $F = 0$, we find that even for the low value of $F = 10$ gravity forms a dominant dipole structure near the emerging cavity at $z = 0$, along with counterrotating shoulder vortices near the lateral symmetry boundaries. For the larger value of $F = 60$, gravity's strong influence is already felt right at the finger tip. The finger tip itself is lifted above the centre plane $y = 0$, and the flow in its vicinity represents a combination of source flow and dipole vortex, cf. the cross-cut in figure 21(*d*). Some distance behind the front, we again recognize the formation of a cavity by a strong vortex dipole, along with counterrotating shoulder vortices near the lateral boundaries.

5.3.1. *Global vorticity dynamics*

In order to identify the dominant features associated with the global dynamics of the vorticity field, it is useful to move beyond a description of the detailed, local aspects of the time-dependent vorticity field. For this purpose, we now focus on the spatiotemporal evolution of averaged quantities. More specifically, we consider
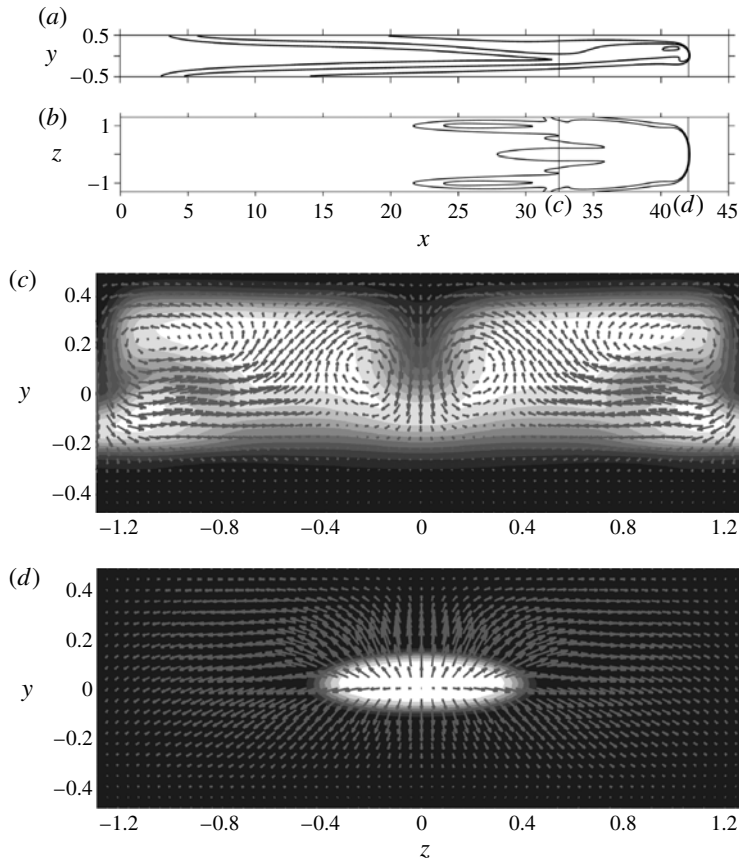
FIGURE 20. Three-dimensional flow evolution for $F = 10$, $R = 2.0$, $Re = e^{-2.0}$ and $Pe = 2000$ at time $t = 25.0$: (*a*) concentration contours $c = 0.1$, 0.5 and 0.9 in the symmetry plane $z = 0$; (*b*) the same concentration contours within the plane of the tip $y = y_{tip}$; (*c,d*) concentration field and (v, w)-velocity vectors at different streamwise locations, (*c*) cut through the cavity at $x = 32.5$ and (*d*) cut near the finger tip at $x = 42.0$.

the (y, z)-averages of the magnitude of the streamwise and gapwise vorticity components, as functions of x and t.

Figure 22(*a*) shows the averaged streamwise vorticity magnitude $\langle|\Omega_x|\rangle_{y,z}(x, t)$ for the relatively low-gravity parameter value of $F = 5$, while figure 22(*b*) provides corresponding information for the average gapwise vorticity magnitude $\langle|\Omega_y|\rangle_{y,z}(x, t)$. The striking similarity between the two figures is consistent with our earlier observation that there exists a strong spatial correlation between these two vorticity components. Both figures indicate the existence of a main vorticity 'front' associated with the A vortices that accompany the advancing finger tip. A secondary front, which originates from approximately the same (x, t)-location, signifies the influence of the shoulder vortices described above. Clearly, these shoulder vortices advance at a lower streamwise velocity as compared with the A vortices. The (x, t)-origin of these two vortex families is determined by the time and x-location at which the two-dimensional base state is first disturbed. The essence of the above information is summarized in the schematic figure 22(*c*).
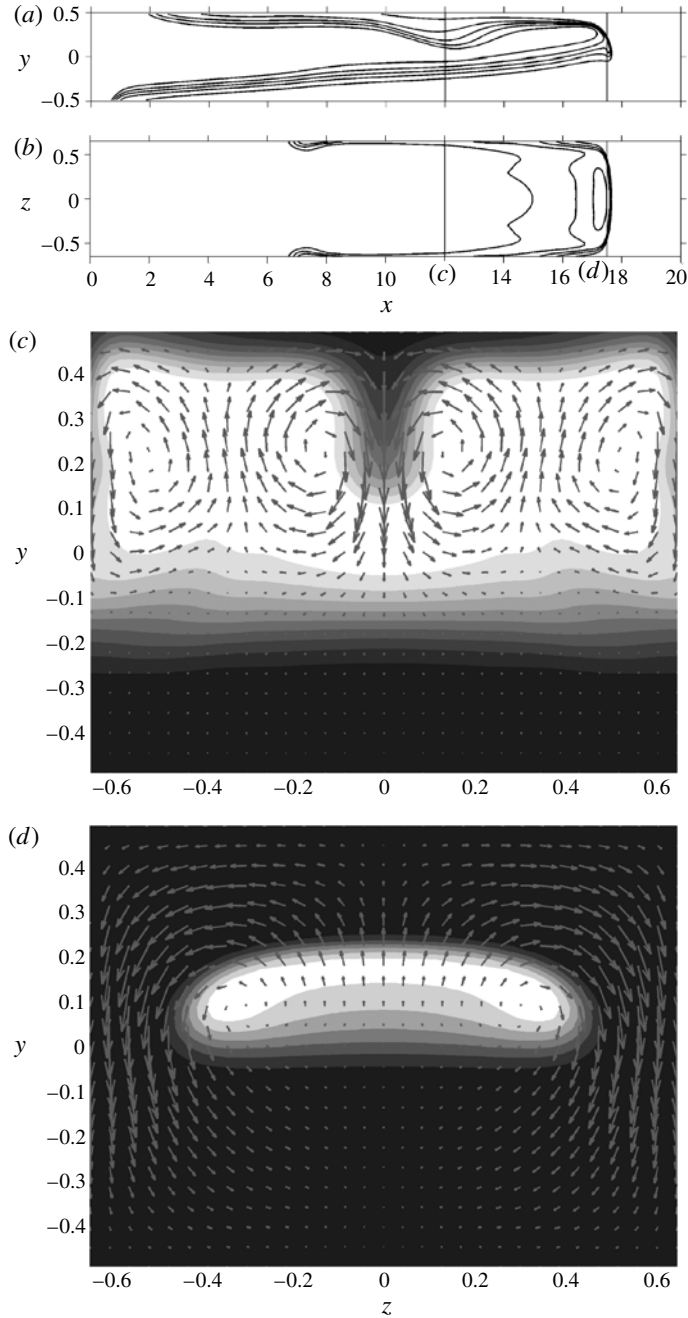
FIGURE 21. Three-dimensional flow evolution for $F = 60$, $R = 2.0$, $Re = e^{-2.0}$ and $Pe = 2000$ at time $t = 10.5$: (*a*) concentration contours $c = 0.1$, 0.5 and 0.9 in the symmetry plane $z = 0$; (*b*) the same concentration contours within the plane of the tip $y = y_{tip}$; (*c*,*d*) concentration field and (v, w)- velocity vectors at different streamwise locations, (*c*) cut through the cavity at $x = 12.0$ and (*d*) cut near the finger tip at $x = 17.5$.
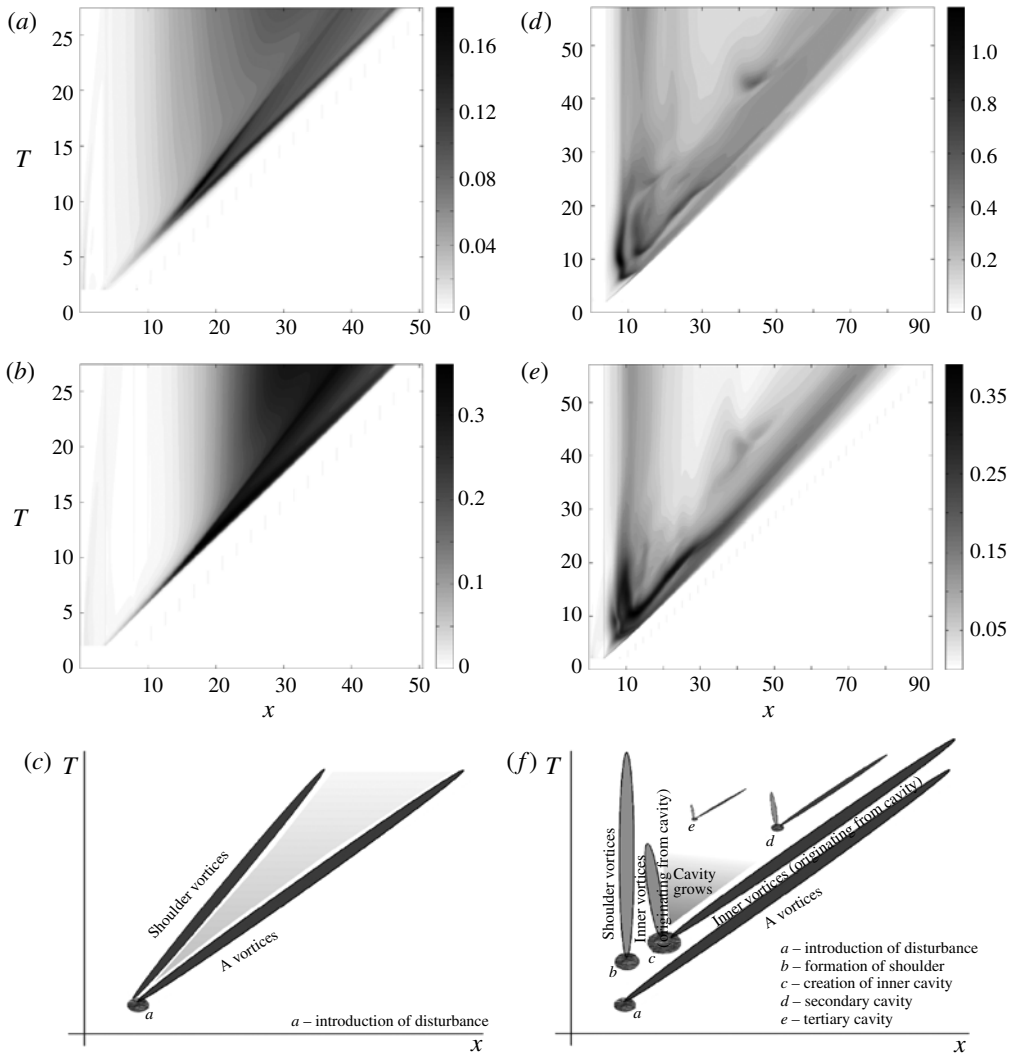
FIGURE 22. Contour plots of the (y, z)-averaged magnitude of the streamwise and gapwise vorticity components, for $R = 2.0$, $Re = e^{-2.0}$, $Pe = 2000$ and $F = 5$ $(a$–$c)$ and $F = 60$ $(d$–$f)$. (a,d) Streamwise component $\langle|\Omega_x|\rangle_{y,z}(x, t)$. (b,e) Gapwise component $\langle|\Omega_y|\rangle_{y,z}(x, t)$. (c,f) Schematic representation. By focusing on the locations where the vorticity has a maximum in the (x, t)-plane, it indicates that the pattern formation is associated with the vorticity dynamics.

Corresponding information for a flow with a larger gravity parameter value of $F = 60$ is provided in figure 22$(d$–$f)$. At this larger value of F, the tendency of gravity to form pronounced shoulder vortices is much stronger than for the lower F-value. In fact, the generation mechanism for the shoulder vortices is so strong that they are not being swept downstream, but rather remain anchored to the location where they first originate. Furthermore, the formation of a cavity near $z = 0$ is observed as well, associated with a dipole of inner vortices. Owing to the strong influence of gravity, this cavity grows rapidly in length. While its leading edge moves at approximately
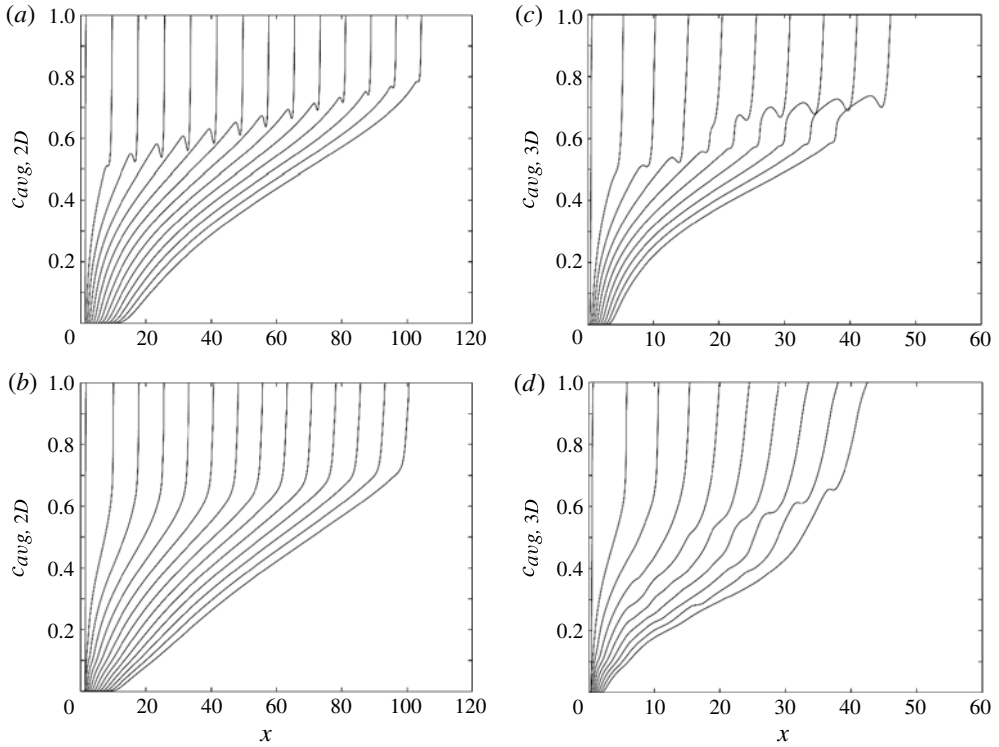
FIGURE 23. The (y, z)-averaged concentration profiles for $R = 2.0$, $Re = e^{-2.0}$ and $Pe = 2000$: (a,c) $F = 0$, (b,d) $F = 60$. (a,b) Two-dimensional simulations at times $t = 0$, 5, 10, ..., 65. (c,d) Three-dimensional simulations at times $t = 0$, 3, 6, ..., 27. For both two- and three-dimensional displacements, the variable density fronts propagate more slowly than the constant density ones, indicating that a higher fraction of the resident fluid is being displaced in the variable density flows.

the same velocity as the finger tip, its trailing edge even moves slightly upstream. Note that gravitational instabilities may form additional, smaller cavities in the upper interface at later times, as indicated by points d and e in the schematic figure 22(f).

We remark that it is not meaningful to draw corresponding figures for the spanwise vorticity component, which is dominated by the Poiseuille base flow component.

5.4. *Cross-section averaged concentration profiles*

Figure 23 displays (y, z)-averaged concentration profiles $c_{avg}(x, t)$ for four different simulations with $R = 2.0$, $Re = e^{-2.0}$ and $Pe = 2000$. Figure 23(a,c) show the neutrally buoyant case $F = 0$, while figure 23(b,d) are for $F = 60$. Two-dimensional simulation results are given in figure 23(a,c), with figure 23(b,d) presenting their three-dimensional counterparts. The two-dimensional, neutrally buoyant results show the formation of a steep shock at the front, consistent with the observations by Lajeunesse *et al.* (1997, 1999). The local minimum immediately behind the front reflects the dispersive pinch-off discussed earlier. The two-dimensional results for $F = 60$ display no such minimum, reflecting the absence of pinch-off. In three dimensions for $F = 0$, both the shoulder as a result of the finger formation, and also the effects of the pinch-off at the finger tip are clearly visible. In the three-dimensional simulation
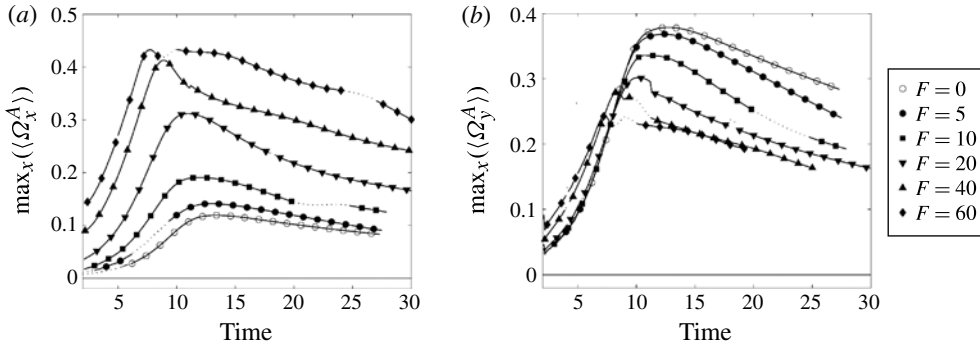
FIGURE 24. Maximum values (—), and interpolated curves ($\cdots$): (*a*) streamwise vorticity component $\max_x(\langle|\Omega_x|\rangle^A_{y,z}(F, t))$; (*b*) gapwise vorticity component $\max_x(\langle|\Omega_y|\rangle^A_{y,z}(F, t))$ for various F, $R = 2.0$, $Re = e^{-2.0}$ and $Pe = 2000$.

for $F = 60$, all of these features get smoothed out somewhat, due to intense mixing of the two fluids in much of the *x*-domain. Note that the three-dimensional front for $F = 60$ moves significantly more slowly than for the corresponding neutrally buoyant case, cf. also figure 15. This demonstrates the higher overall displacement efficiency of the $F = 60$ case, indicating that the resident fluid is driven out of the Hele-Shaw cell more completely for variable density displacements than for neutrally buoyant cases. This observation is potentially significant for those applications in enhanced oil recovery for which displacements within hydraulically opened fractures play an important role.

5.5. *Transition from viscous finger tip to gravitational finger tip*

The viscous fingering instability leads primarily to the formation of gapwise vorticity, while gravity is the main driver responsible for the generation of streamwise vorticity. Hence, a comparison of the two components can determine which of the two effects dominates. To this end, figure 24 provides data for the *A* vortices, as a function of time and *F*. Specifically, figure 24(*a*) shows the transient growth and decay of the maximum value (over *x*) of the (y, z)-averaged streamwise vorticity magnitude, $\max_x(\langle|\Omega_x|\rangle^A_{y,z})(t)$. Figure 24(*b*) indicates corresponding information for the maximum value of the (y, z)-averaged gapwise vorticity magnitude, $\max_x(\langle|\Omega_y|\rangle^A_{y,z})(t)$. Near locations where vortex branching occurs, it was occasionally not possible to identify a maximum of the *A* vorticity, so that we fitted the curve by using interpolation.

In general, larger gravity numbers result in stronger streamwise and weaker gapwise vorticity components. The temporal evolution of both components is qualitatively similar for all *F*-values, displaying transient growth followed by monotonic decay. We define the ratio $a(F, t)$ of the two maximum values as

$$a(F, t) = \frac{\max_x(\langle|\Omega_y|\rangle^A_{y,z}(x, t, F))}{\max_x(\langle|\Omega_x|\rangle^A_{y,z}(x, t, F))}. \tag{5.1}$$

We remark that the limits of *a* for purely viscous or gravitational instability are not well defined, since both vorticity components are non-zero in both cases. Figure 25(*a*) shows $a(F, t)$ for $R = 2.0$, $Re = e^{-2.0}$ and $Pe = 2000$, where those values corresponding to the fitted curve sections above are indicated by dashed lines.
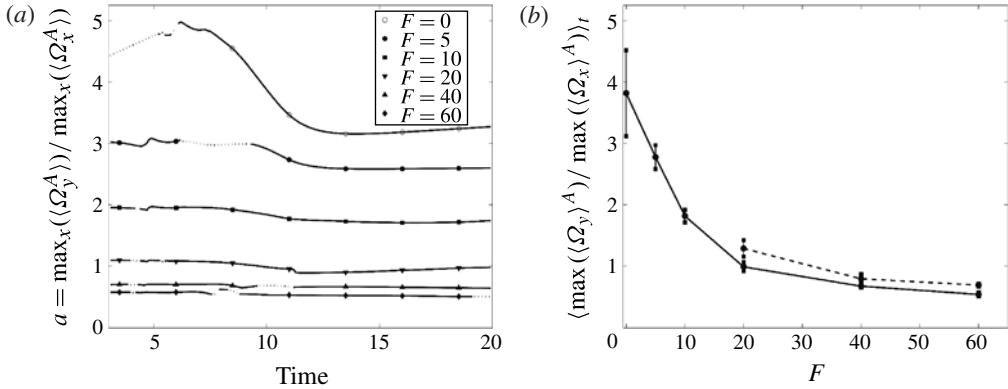
FIGURE 25. (a) Ratio $a(F, t)$ of the maxima of gapwise to streamwise averaged A vorticity as a function of F and t, for $R = 2.0$, $Re = e^{-2.0}$ and $Pe = 2000$: (——) where calculated from maxima; (- - -) where calculated from fitted values. (b) Time-averaged ratio $\langle a(F, t) \rangle_t (F)$ as a function of F, for $R = 2.0$ (——) and $R = 2.5$ (- - -). The error bars indicate the standard deviation from the averaged values.

As F is increased from 0 to 60, $a(F, t)$ decreases by almost an order of magnitude, indicating that streamwise vorticity is becoming more dominant. We note that for sufficiently large F-values, $a(F, t)$ remains nearly constant over time, which shows that the growth and decay of the two A vorticity components does not exhibit a phase lag. Only for very small F-values does a time dependence of $a(F, t)$ persist, showing faster growing gapwise vorticity initially. Later, the gapwise vorticity already decays, while the streamwise vorticity is still growing. Eventually, both decay rates become equal, see figure 25(b).

6. Summary and conclusions

The present investigation has employed direct numerical simulations of the variable density and viscosity Navier–Stokes equations, in order to explore three-dimensional effects within miscible displacements in horizontal Hele-Shaw cells. These simulations identify a number of mechanisms that cannot be analysed based on gap-averaged approaches.

Regarding the long-term evolution of the two-dimensional base states, we find that the tendency of the early, quasisteady phase investigated by Talon *et al.* (2013) is reversed, in that fronts propagate more slowly for stronger density contrasts. The two-dimensional simulations furthermore show that, in addition to the dispersive pinch-off immediately behind the front for low F-values, a larger-scale gravitational pinch-off can occur far behind the front for higher F-values. This gravitational pinch-off effectively cuts the front off from its supply of injected fluid and allows it to rise in response to buoyancy forces.

Three-dimensional simulations reveal the mechanisms by which the viscous fingering instability interacts with a spanwise Rayleigh–Taylor instability. Consistent with the linear stability results of Talon *et al.* (2013), we observe that the dominant wavelength of the Rayleigh–Taylor instability is shorter than that of the fingering instability. This results in the formation of negatively buoyant plumes of the more viscous resident fluid not only in between neighbouring viscous fingers, but also along

the centre of the finger. In this way, a streamwise cavity forms along the axis of the viscous finger, which can result in its longitudinal splitting.

The negatively buoyant plumes are associated with streamwise vorticity dipoles, rather than the quadrupoles observed by Oliveira & Meiburg (2011) for constant density displacements. They can destroy the shoulders connecting neighbouring fingers, thereby increasing the effective length of the viscous fingers. We note that the formation of the streamwise cavity in three-dimensional flows typically occurs earlier than the gravitational pinch-off of the corresponding two-dimensional base state, so that this pinch-off may not be observed in experiments. On occasion, we have also observed that neighbouring fingers can reconnect some distance downstream of their original shoulder, as a result of spanwise transport of injected fluid, trapping resident fluid in the process.

In analysing the streamwise and gapwise vorticity components, we found that these exhibit a strong spatial correlation. The streamwise vorticity dipoles forming as a result of the spanwise Rayleigh–Taylor instability place viscous resident fluid in between regions of less viscous, injected fluid. This results in the formation of gapwise vorticity at the same location via the traditional, gap-averaged viscous fingering mechanism. Both the streamwise and the gapwise vorticity components in the dominant vortical structures first grow and then decay exponentially over time. For larger F-values, the streamwise vorticity component increases, while the gapwise component is reduced, thus indicating a transition from viscously dominated to gravitationally dominated fingers.

Gap-averaged, time-dependent concentration profiles reflect the vigorous mixing observed in three-dimensional displacements, as a result of gravitational effects. They furthermore show that for both two- and three-dimensional flows, variable density displacement fronts propagate more slowly than their constant density counterparts. This indicates that the gravitational mixing results in a more complete expulsion of the resident fluid from the Hele-Shaw cell. This observation may be of interest in the context of enhanced oil recovery or carbon sequestration applications involving displacements in hydraulically opened fractures, which share features with Hele-Shaw displacements.

Acknowledgements

REFERENCES

AUBERTIN, A., GAUTHIER, G., MARTIN, J., SALIN, D. & TALON, L. 2009 Miscible viscous fingering in microgravity. *Phys. Fluids* **21** (054107).

FERNANDEZ, J., KUROWSKI, P., PETITJEANS, P. & MEIBURG, E. 2002 Density-driven unstable flows of miscible fluids in a Hele-Shaw cell. *J. Fluid Mech.* **451**, 239–260.

GONDRET, P. & RABAUD, M. 1997 Shear instability of two-fluid parallel flow in a Hele-Shaw cell. *Phys. Fluids* **9** (11), 3267–3274.

GOYAL, N. & MEIBURG, E. 2004 Unstable density stratification of miscible fluids in a vertical Hele-Shaw cell: influence of variable viscosity on the linear stability. *J. Fluid Mech.* **516**, 211–238.

GOYAL, N. & MEIBURG, E. 2006 Miscible displacements in Hele-Shaw cells: two-dimensional base states and their linear stability. *J. Fluid Mech.* **558**, 329–355.

GOYAL, N., PICHLER, H. & MEIBURG, E. 2007 Variable-density miscible displacements in a vertical Hele-Shaw cell: linear stability. *J. Fluid Mech.* **584**, 357–372.

GRAF, F., MEIBURG, E. & HÄRTEL, C. 2002 Density-driven instabilities of miscible fluids in a Hele-Shaw cell: linear stability analysis of the three-dimensional Stokes equations. *J. Fluid Mech.* **451**, 261–282.

HALLEZ, Y. & MAGNAUDET, J. 2008 Effects of channel geometry on buoyancy-driven mixing. *Phys. Fluids* **20** (053306).

HARTEL, C., MEIBURG, E. & NECKER, F. 2000 Analysis and direct numerical simulation of the flow at a gravity-current head. Part 1. Flow topology and front speed for slip and no-slip boundaries. *J. Fluid Mech.* **418**, 189–212.

HOMSY, G. M. 1987 Viscous fingering in porous media. *Annu. Rev. Fluid Mech.* **19**, 271–311.

JIANG, G.-S. & PENG, D. 2000 Weighted ENO schemes for Hamilton Jacobi equations. *SIAM J. Sci. Comput.* **21** (6), 2126–2143.

KIM, J. & MOIN, P. 1985 Application of a fractional-step method to incompressible Navier–Stokes equations. *J. Comput. Phys.* **59**, 308–323.

LAJEUNESSE, E., MARTIN, J., RAKOTOMALALA, N. & SALIN, D. 1997 3D instability of miscible displacements in a Hele-Shaw cell. *Phys. Rev. Lett.* **79** (26), 5254–5257.

LAJEUNESSE, E., MARTIN, J., RAKOTOMALALA, N. & SALIN, D. 2001 The threshold of the instability in miscible displacement in a Hele-Shaw cell at high rates. *Phys. Fluids* **13** (3), 799.

LAJEUNESSE, E., MARTIN, J., RAKOTOMALALA, N., SALIN, D. & YORTSOS, Y. C. 1999 Miscible displacement in a Hele-Shaw cell at high rates. *J. Fluid Mech.* **398**, 229–319.

MARTIN, J., RAKOTOMALALA, N & SALIN, D. 2002 Gravitational instability of miscible fluids in a Hele-Shaw cell. *Phys. Fluids* **14** (2), 902–905.

MAXWORTHY, T. 1987 The nonlinear growth of a gravitationally unstable interface in a Hele-Shaw cell. *J. Fluid Mech.* **177**, 207–232.

MCLEAN, J. W. & SAFFMAN, P. G. 1981 The effect of surface tension of the shape of fingers in a Hele-Shaw cell. *J. Fluid Mech.* **102**, 261–282.

MEIBURG, E. & HOMSY, G. M. 1988 Nonlinear unstable viscous fingers in Hele-Shaw flows. II. Numerical simulation. *Phys. Fluids* **31**, 429–439.

OLIVEIRA, R. M. 2012 Three-dimensional Navier–Stokes simulations of miscible displacements in Hele-Shaw cells. PhD thesis, UCSB.

OLIVEIRA, R. M. & MEIBURG, E. 2011 Miscible displacements in Hele-Shaw cells: three-dimensional Navier–Stokes simulations. *J. Fluid Mech* **687**, 431–460.

PARK, C. W. & HOMSY, G. M. 1984 Two-phase displacement in Hele-Shaw cells: theory. *J. Fluid Mech.* **139**, 291–308.

PETITJEANS, P., CHEN, C. Y., MEIBURG, E. & MAXWORTHY, T. 1999 Miscible quarter five-spot displacements in a Hele-Shaw cell and the role of flow-induced dispersion. *Phys. Fluids* **11** (7), 1705–1716.

PETITJEANS, P. & MAXWORTHY, T. 1996 Miscible displacements in capillary tubes. Part 1. Experiments. *J. Fluid Mech.* **326**, 37–56.

PLOURABOUÉ, F. & HINCH, E. J. 2002 Kelvin–Helmholtz instability in a Hele-Shaw cell. *Phys. Fluids* **14** (3), 922–929.

RAI, M. M. & MOIN, P. 1991 Direct simulations of turbulent flow using finite-difference schemes. *J. Comput. Phys.* **96** (1), 15–53.

SAFFMAN, P. G. & TAYLOR, G. I. 1958 The penetration of a fluid into a porous medium or Hele-Shaw cell containing a more viscous liquid. *Proc. R. Soc. Lond. Ser.* A **245**, 312–329.

SÉON, T., HULIN, J.-P. & SALIN, D. 2005 Buoyancy driven miscible front dynamics in tilted tubes. *Phys. Fluids* **17** (031702).

SÉON, T., HULIN, J.-P., SALIN, D., PERRIN, B. & HINCH, E. J. 2006 Laser-induced fluorescence measurements of buoyancy driven mixing in tilted tubes. *Phys. Fluids* **18** (041701).

SÉON, T., ZNAIEN, J., PERRIN, B., HINCH, E. J., SALIN, D. & HULIN, J. P. 2007 Front dynamics and macroscopic diffusion in buoyant mixing in a tilted tube. *Phys. Fluids* **19** (125105).

SIMPSON, J. E. 1997 *Gravity Currents in the Environment and the Laboratory*, 2nd edn. Cambridge University Press.

TAGHAVI, S. M., ALBA, K., SEON, T., WIELAGE-BURCHARD, K., MARTINEZ, D. M. & FRIGAARD, I. A. 2011a Miscible displacement flows in near-horizontal ducts at low atwood number. *J. Fluid Mech.* **696**, 175–214.

TAGHAVI, S. M., SEON, T., MARTINEZ, D. M. & FRIGAARD, I. A. 2010 Influence of an imposed flow on the stability of a gravity current in a near horizontal duct. *Phys. Fluids* **22** (3), 031702.

TAGHAVI, S. M., SEON, T., WIELAGE-BURCHARD, K., MARTINEZ, D. M. & FRIGAARD, I. A. 2011b Stationary residual layers in buoyant Newtonian displacement flows. *Phys. Fluids* **23** (4), 044105.

TALON, L., GOYAL, N. & MEIBURG, E. 2013 Variable density and viscosity, miscible displacements in horizontal Hele-Shaw cells. Part 1. Linear stability analysis. *J. Fluid Mech.* **721**, 268–294.

TAN, C. T. & HOMSY, G. M. 1988 Simulation of nonlinear viscous fingering in miscible displacement. *Phys. Fluids* **31** (6), 1330–1338.

TAYLOR, G. 1953 Dispersion of soluble matter in solvent flowing slowly through a tube. *Proc. R. Soc. Lond. Ser.* A **219** (1137), 186–203.

VANAPARTHY, S. H. & MEIBURG, E. 2008 Variable density and viscosity, miscible diplacements in capillary tubes. *Eur. J. Mech.* B/*Fluids* **27**, 268–289.

WOODING, R. A. 1969 Growth of fingers at an unstable diffusing interface in a porous medium or Hele-Shaw cell. *J. Fluid Mech.* **39**, 477–495.